Alexandria Engineering Journal (2023) 69, 9–24

HOSTED BY

ELSEVIER

Alexandria University

Alexandria Engineering Journal

www.elsevier.com/locate/aej
www.sciencedirect.com

ORIGINAL ARTICLE

Modeling and simulation of blood flow under the influence of radioactive materials having slip with MHD and nonlinear mixed convection

Sidra Afzal [a], Mubashir Qayyum [a], Muhammad Bilal Riaz [b,c,*], Adam Wojciechowski [d]

[a] *National University of Computer and Emerging Sciences FAST Lahore, Pakistan*
[b] *Faculty of Applied Physics and Mathematics, Gdansk University of Technology, Gabriela Narutowicza 11/12, 80-233 Gdańsk, Poland*
[c] *Department of Mathematics, University of Management and Technology, C-II Joar Town 54770 Lahore, Pakistan*
[d] *Faculty of Technical Physics, Information Technology and Applied Mathematics, Lodz University of Technology, 90-924 Lodz, Poland*

Received 24 October 2022; revised 23 December 2022; accepted 7 January 2023

KEYWORDS

Nanofluid;
Mixed convection;
Joule heating;
Thermal radiation;
Velocity and temperature slip

Abstract Radioactive materials are widely in industry, nuclear plants and medical treatments. Scientists and workers in these fields are mostly exposed to such materials, and adverse effects on blood and temperature profiles are observed. In this regard, objective of the current study is to model and simulate blood based nanofluid with three very important radioactive materials, named as Uranium dioxide (UO_2), Thorium dioxide (ThO_2) and Radium (Rd). In this modeling blood based nanofluid is considered under the influence of magneto hydrodynamic effect, non-linear mixed convection and thermal radiation, Joule heating, along with velocity and temperature slip. A three-dimensional fluid model is considered in bounded domain to justify flow geometry in arteries. System of partial differential equations are converted to highly nonlinear coupled ordinary differential equations by using suitable transformations. The obtained system is solved numerically using Fehlberg Runge–Kutta algorithm. Validity and convergence of the obtained solutions are confirmed through residual errors, numerical uncertainties and comparison with experimental data. Moreover, effect of pertinent fluid parameters on the velocity (radial, axial, tangential) and temperature profiles of blood flow are analyzed graphically. Furthermore, Skin friction and Nusselt number are also analyzed graphically against volume fraction of involved radioactive materials for the case of UO_2, ThO_2 and Rd comparatively. Analysis reveals that increase in volume fraction of radioactive elements results in increased blood flow through walls in both radial and tangential

* Corresponding author.
E-mail address: bilalsehole@gmail.com (M.B. Riaz).
Peer review under responsibility of Faculty of Engineering, Alexandria University.

https://doi.org/10.1016/j.aej.2023.01.013

Nomenclature

(u, v, w)	Velocity components
(r, ϕ, z)	Cylindrical coordinates
T	Fluid temperature
T_1, T_2	Temperature of lower wall, upper wall
γ_1, γ_2	Velocity, temperature slip factor
w_0	Suction/Injuction in z-direction
l	Distance between the walls
f, nf, s	base fluid, nanofluid, solid nanoparticle quantity
B_0	Magnetic field strength
φ	Nanoparticle volume fraction
$\rho_f, \rho_{nf}, \rho_s$	Density
α_{nf}	Thermal diffusivity
$(\rho Cp)_f, (\rho Cp)_{nf}$	Heat capacitance
g	Gravitational acceleration
ν_f, ν_{nf}	Kinematic viscosity
μ_f, μ_{nf}	Dynamic viscosity
σ_f, σ_{nf}	Electrical conductivity
k_f, k_{nf}	Effective thermal conductivity
α_1, α_2	linear, non-linear thermal expansion
q_r	Radiative heat flux
M	Magnetic interaction parameter
Pr, Ec	Prandtl number, Eckert number
λ_1, λ_2	Linear, non-linear mixed convection parameters
θ_ω	Temperature ratio parameter
$\widetilde{R}$	Radiation parameter
ϵ_i	Dimensionless nanofluid parameters
$\tau_{wr}, \tau_{w\phi}$	Transversal and radial shear stress
q_w	Heat flux at wall
Re	Local Reynolds number
C_f, Nu	Skin friction, Nusselt number
$\mathfrak{U}_c$, μ_i, n	Uncertainty, Mean, No. of iterations

directions. In case of slip at fluid solid-interface, the highest skin fraction is observed in case of Radium nanoparticles.

1. Introduction

Study of non-Newtonian fluid models to better understand blood flow problems have been done in literature. It became easier to model blood flow problems and encompass effects important in human body to such problems. In recent studies, nanofluid has gathered much importance due to its effectiveness in capturing many physical phenomenon [1–3]. But an important fact that needs to be catered is the effect of various radioactive material on blood considered as base fluid in nanofluid, which is main focus of this study. Blood with various other nanoparticles have been studied in literature by many researchers. Basha and Sivaraj [4] studied blood nanofluid in three geometries. Hybrid blood nanofluid with MHD effect is studied by Alghamdi et al. [5]. Shah et al. investigated gold particle blood nanofluid under radiative heat transfer [6]. Biswas et al. [7] simulated a water based nanofluid with copper nanoparticles and oxytactic bacteria in a W-Shaped porous cavity under impact of perpendicular magnetic field and three types of convection. TiO/Ag nanofluid with blood as base fluid for drug transport through arteries was analyzed by Chahregh and Dinarvend [8].

MHD plays a vital role when treating maligns and cancer, drug targeting, cell separation, magnetic endoscopy and adjusting blood flow during surgery. Behavior of blood flow and temperature is essential to be studied for having more controlled environment during such processes. Prakash et al. [9] studied MHD effects on bifurcated arteries. Barnoon and Ashkiyan [10] presented numerical study on the magnetic field generation in the microwave technique for non-surgical treatment of liver tumors. Mondal et al. [11] investigated flow in a $Cu - Al_2O_3$ hybrid nanofluid on a magnetic porous wall with partial translation in order to enhance the rate of heat transfer. Radiative MHD flow in a rotating cone with Soret and Dufour effects is studied by Khan et al. [12]. Analysis on flow of a hybrid nanofluid magnetized horizontally in an M-shaped non-Darcian cavity is presented by Mandal et al. [13]. Barnoon et al. [14] analyzed effect of diameter of nanoparticles on entropy generation and heat transfer rates in nanofluids with single and two phase models under impact of magnetic field. Anuar et al. [15] analytically studied MHD flow in carbon tubes with stability analysis.

The flow under mixed convection is prominent in many industrial, engineering and natural processes. In case of thermal equipment in industries and nuclear plants, high temperature is required for proper operation. This causes non-linearity among temperature and density which is dependent on fluid concentration. Mostly in literature non-linear mixed convection is ignored due to high non-linearity and computational cost in problem solving. In case of radioactive blood-nanofluid flow, mixed convection is added in this study for more general and comprehensive results. Xia et al. [16] investigated non-linear mixed convection on hybrid nanofluid for multiple slip boundary conditions. Micropolar nanofluid over non-isothermal sphere under MHD nonlinear mixed convection was characterized by Ibrahim and Zemedu [17]. Mandal et al. [18] investigated a hybrid nanofluid flow with copper and aluminum oxide nanoparticle within a porous cavity effected by mixed convection and magnetohydrodynamic force. Irfan et al. [19] studied 3D Carreau nanofluid under influence of non-linear thermal radiation and Arrhenius activation energy. Effect of magnetic and thermal convection on flow of a hybrid nanofluid through a complex wavy enclosure is considered by Mandal et al. [20]. Darcy Forchheimer flow with chemical reaction, non-linear mixed convection and stretching is analyzed by Hayat et al. [21].

The model considered, contains radioactive material as nanoparticles, hence it becomes much important to incooperate non-linear thermal radiation. Non-linear thermal radiation plays a vital role in heat transfer and is studied by many researchers in physics and engineering fields[22–25]. Maxwell nanofluid in a stretching cylinder with activation energy and nonlinear mixed convection was studied by Li et al. [26]. Muhammad et al. investigated nanofluid heat transport on quadratic stretching plate with non-linear thermal radiation [27]. Barnoor [28] investigated the rate of heat transfer in a hybrid nanofluid flow through a dual mixer microchannel equipped with four pair of electrodes. Carreau nanofluid with bioconvection transport under effect of non-linear thermal radiation is examined by Imran et al. [29]. Song et al. [30] analyzed micropolar nanofluid on an off centered rotating disk with Darcy's law and non-linear thermal radiation. Ijaz et al. [31] studied micropolar nanofluid in porous rotating disk with microorganisms and non-linear radiation. Barnoon and Bakhshandehfard [32] analyzed thermal management perspective of destroying a liver tissue with local heating. Bilal et al. [33] did entropy optimization on Williamson nanofluid with non-linear thermal radiation with non Darcian MHD.

Velocity without slip conditions is considered when velocity of fluid and the wall is same. But when fluid velocity becomes different from velocity of the wall, then slip velocity is considered. Similarly, in case of temperature slip, the fluid temperature and wall temperature is different. This phenomena is much significant in medical industry as it is useful in improving artificial interior cavities and heart valves. Sajid et al. [34] scrutinized Maxwell velocity slip and Smoluchowski temperature slip on Reiner-Philoppoff fluid model. Khan and Rasheed [35] employed velocity and thermal slip on MoS_2-SiO_2 hybrid nanofluid. Two-phase fluid flow with temperature slip boundary conditions is studied by Xiong et al. [36]. Hayat et al. [37] also investigated velocity slip with dissipation in a stretching cylinder.

Main aim of this manuscript is to study the effects of radioactive nanoparticles on blood flow. Various studies have been done on blood nanofluid in literature, but effects of radioactive material on blood phase has not been investigated and especially not with the further mentioned effects and boundary conditions. In this regard, the current flow problem is captured by considering blood phase as base fluid with three types of radioactive materials taken as nanoparticles UO_2, ThO_2 and Rd. Additional effects on velocity, temperature and boundary are also added to capture a more general phenomena. The fluid model is devised in cylindrical coordinates (depicting blood arteries) with magnetohydrodynamic effect, non-linear mixed convection, Joule heating, non-linear thermal radiation, suction/injuction, porous medium, velocity and temperature slip boundary conditions. The system of partial differential equations is converted to system of ordinary differential equations using similarity transformations. Fehlberg RK method is used to solve the equations and errors are depicted for convergence analysis of fluid model. Comparison of present results with experimental data in literature is also presented. It is observed that the current results are in good agreement with experimental results which provides further validation. Skin friction and Nusselt number on both walls are analyzed graphically and compared for each nanoparticle UO_2, ThO_2 and Rd, separately. Dimensionless parameters are varied to study effects on radial, axial, tangential velocity and temperature profiles. Furthermore, contour plots are presented for prediction of blood flow and temperature regime in the modeled physical environment. Further manuscript is categorized as follows: Section 2 presents formulation of the problem, Section 3 shows skin friction and Nusselt number at both walls, in Section 5 discussion on results is presented and Section 6 contains conclusion of the manuscript.

2. Model formulation

Consider the laminar, axially symmetric, two-dimensional flow geometry in cylindrical coordinates (r, ϕ, z) of an incompressible nanofluid through an artery. It is assumed that channel is porous and MHD effect is in z-direction. The non-linear mixed convection and thermal radiation with Joule heating is considered. Velocity and temperature slip taken at the boundary $z = 0$. Geometry of the flow can be seen in Fig. 1. Governing equations for the given phenomena are as follows:

$$u_r + \frac{u}{r} + w_z = 0, \tag{1}$$

$$uu_r + wu_z - \frac{v^2}{r} = \nu_{nf}\nabla^2 u - \frac{\sigma_{nf}B_0^2}{\rho_{nf}}u + \rho_{nf}g\left\{\alpha_1(T - T_2) + \alpha_2(T - T_2)^2\right\}, \tag{2}$$

$$uv_r + wv_z + \frac{uv}{r} = \nu_{nf}\nabla^2 v - \frac{\sigma_{nf}B_0^2}{\rho_{nf}}v, \tag{3}$$

$$uT_r + wT_z = \alpha_{nf}\nabla^2 T + \frac{1}{(\rho C_p)_{nf}}\sigma_{nf}B_0^2\left(v^2 + u^2\right) - \frac{1}{(\rho C_p)_{nf}}(q_r)_z, \tag{4}$$

subject to following appropriate boundary conditions

$$u = \gamma_1 u'(0), \quad v = \omega r, \quad w = w_0 \quad T = T_1 + \gamma_2 T_1'(0), \quad at \quad z = 0 \quad u = 0, \quad v = 0, \quad T = T_2, \quad at \quad z = l \tag{5}$$

where u, v and w are velocity components in r, ϕ and z-direction respectively, and T is the fluid temperature. A constant magnetic field B_0 is applied in vertical direction normal to surface $z = 0$. Injection w_0 is taken in z-direction. Rotation $r\omega$ takes place in ϕ-direction. In (2), α_1 and α_2 are linear and non-linear thermal expansion coefficients.The quantity $(q_r)_z$ on right-hand side of (4) and all nanofluid quantities in (1)–(4) are given in (6).

$$\alpha_{nf} = \frac{k_{nf}}{(\rho C_p)_{nf}}, \quad \nu_{nf} = \frac{\mu_{nf}}{\rho_{nf}}, \quad \rho_{nf} = (1-\varphi)\rho_f + \varphi\rho_s, \quad \mu_{nf} = \frac{\mu_f}{(1-\varphi)^{2.5}},$$
$$(\rho C_p)_{nf} = (1-\varphi)(\rho C_p)_f + \varphi(\rho C_p)_s, \quad \frac{k_{nf}}{k_f} = \frac{(k_s+2k_f) - 2\varphi(k_f - k_s)}{(k_s+2k_f) + \varphi(k_f - k_s)},$$
$$\frac{\sigma_{nf}}{\sigma_f} = 1 + \frac{3\left(\frac{\sigma_s}{\sigma_f} - 1\right)\varphi}{\left(\frac{\sigma_s}{\sigma_f} + 2\right) - \left(\frac{\sigma_s}{\sigma_f} - 1\right)\varphi}, \quad q_r = \frac{-4\sigma^*}{3k^*}\frac{\partial T^4}{\partial z} = \frac{-16\sigma^*}{3k^*}T_2^3\frac{\partial T}{\partial z}, \tag{6}$$

where, φ is the volume fraction of nanoparticles in base fluid, k_f and k_s is effective thermal conductivity of fluid base and nanoparticles, respectively, ρ_s is the nanoparticle density, ρ_f is the density of fluid base and $(\rho C_p)_{nf}$ is the nanofluid heat

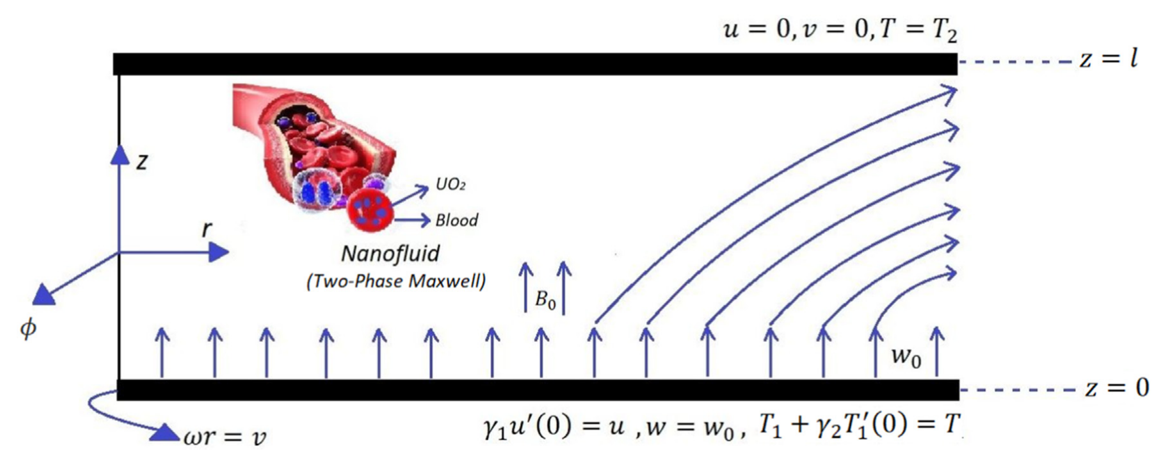

Fig. 1 Flow geometry.

Table 1 Thermophysical Properties of base fluid and nanoparticles [38].

Physical Properties	Blood	UO_2	ThO_2	Rd
$\rho(g/m^3)$	1.050	10.97	11.7	5.5
$C_p(J/gK)$	3.617	235	0.12	0.12
$k(W/mK)$	0.52	8.68	4.3–77.3	19
$\sigma(S/m)$	0.012	0.029	0.054	1×10^6

capacitance. Thermophysical properties of blood (base fluid) and various radioactive particles (Uranium Dioxide/Thorium Dioxide/Radium) is given in Table 1 [38].

We introduce following similarity transformations introduced by Von-Karman for exact and self similar solution of Navier–Stokes equations

$$\eta = \left(\frac{\omega}{v_f}\right)^{\frac{1}{2}} z, \quad u = \omega r F(\eta), \quad v = \omega r G(\eta),$$
$$w = (\omega v_f)^{\frac{1}{2}} H(\eta), \quad \theta(\eta) = \frac{T - T_2}{T_1 - T_2} \tag{7}$$

by applying (7) in (1)–(5) we obtain system of ordinary differential equations as

$$H' + 2F = 0 \tag{8}$$

$$F^2 + HF' - G^2 - \epsilon_5 F'' + \frac{\epsilon_4}{\epsilon_2} MF - \lambda_1 (1 + \lambda_2 \theta)\theta = 0 \tag{9}$$

$$2FG + HG' - \epsilon_5 G'' + \frac{\epsilon_4}{\epsilon_2} MG = 0 \tag{10}$$

$$\frac{1}{Pr}\frac{\epsilon_3}{\epsilon_1}\theta'' - H\theta\prime - \frac{\widetilde{R}}{\epsilon_1 Pr}$$
$$\times \left[(\theta_\omega - 1)^3 \left(3\theta^2\theta'2 + \theta''\theta^3\right) + 3(\theta_\omega - 1)^2\left(2\theta\theta'2 + \theta^2\theta''\right) + 3(\theta_\omega - 1)(\theta'2 + \theta\theta\prime) + \theta''\right]$$
$$+ \frac{\epsilon_4}{\epsilon_1} MEc\left(F^2 + G^2\right)$$
$$= 0 \tag{11}$$

and dimensionless conditions become

$$F(0) = \gamma_1 F\prime(0), \quad G(0) = 1$$
$$H(0) = W_s, \quad \theta(0) = 1 + \gamma_2 \theta\prime(0) \tag{12}$$
$$F(1) = 0, \quad G(1) = 0, \quad \theta(1) = 0$$

In (8)–(12) the dimensionless parameters are

$$M = \frac{\sigma_f B_0^2}{\rho_f \omega}, \quad Pr = \frac{(\rho C_p)_f v_f}{k_f}, \quad Ec = \frac{\omega^2 r^2}{(\rho C_p)_f (T_1 - T_2)}, \quad \lambda_1 = \frac{g\alpha_1}{\omega^2 r}(T_1 - T_2),$$
$$\lambda_2 = \frac{\alpha_2}{\alpha_1}(T_1 - T_2), \quad \widetilde{R} = \frac{16\sigma^* T_2^3}{3k^* k_f}, \quad \theta_\omega = \frac{T_1}{T_2}, \quad \epsilon_1 = \frac{(\rho C_p)_{nf}}{(\rho C_p)_f} = (1 - \varphi) + \frac{(\rho C_p)_s}{(\rho C_p)_f}\varphi,$$
$$\epsilon_2 = \frac{\rho_{nf}}{\rho_f} = (1 - \varphi) + \varphi\frac{\rho_s}{\rho_f}, \quad \epsilon_3 = \frac{k_{nf}}{k_f}, \quad \epsilon_4 = \frac{\sigma_{nf}}{\sigma_f}, \quad \epsilon_5 = \frac{v_{nf}}{v_f} = \frac{1}{(1-\varphi)^{2.5}\left[(1-\varphi) + \varphi\left(\frac{\rho_s}{\rho_f}\right)\right]} \tag{13}$$

where M is the magnetic interaction parameter, Pr is the Prandtl number, Ec is the Eckert number, λ_1 and λ_2 are the linear and non-linear mixed convection parameters, $\widetilde{R}$ is the radiation parameter, θ_ω is the temperature parameter and ϵ_1-ϵ_5 are non-dimensional nanofluid parameters.

3. Skin friction and Nusselt number

Physical quantities, skin friction and Nusselt number are given as

$$C_f = \frac{\sqrt{\tilde{\tau}_{wr}^2 + \tilde{\tau}_{w\phi}^2}}{\rho_f (\omega r)^2}, \quad Nu = \frac{r\tilde{q}_w}{k_f(T_1 - T_2)} \tag{14}$$

$\tilde{\tau}_{wr}$ and $\tilde{\tau}_{w\phi}$ in (14) are radial and transversal skin friction which are basically shear stresses at the boundary.

$$\tilde{\tau}_{wr} = \left[\mu_{nf}(u_z + u_\phi)\right]_{z=0}, \quad \tilde{\tau}_{w\phi} = \left[\mu_{nf}\left(v_z + \tfrac{1}{r} + w_\phi\right)\right]_{z=0},$$
$$\tilde{q}_w = -k_{nf}(T_z)_{z=0}, \tag{15}$$

By using (15) in (14) we obtain (16)

$$Re^{\frac{1}{2}} C_f = \frac{\sqrt{F'(0)^2 + G'(0)^2}}{(1 - \varphi)^{2.5}},$$
$$Re^{\frac{1}{2}} Nu = -\left(\epsilon_3 + \widetilde{R}\right)\theta'(0), \tag{16}$$

here $Re = \frac{\omega r^2}{\nu_f}$ is the local Reynolds number. Similarly, in case of other wall at $\eta = 1$, the skin friction and heat transfer is given in (17)

$$Re^{\frac{1}{2}} C_f = \frac{\sqrt{F\prime(1)^2 + G'(1)^2}}{(1-\varphi)^{2.5}},$$
$$Re^{\frac{1}{2}} Nu = -\left(\epsilon_3 + \widetilde{R}\right)\theta'(1), \tag{17}$$

4. Numerical simulations and convergence

4.1. Solution mechanism

System of ODEs along with boundary conditions in (8)–(12) are solved using Fehlberg Runge–Kutta method. For this scheme we rewrite governing dimensionless equations as

$$\frac{dH(\eta)}{d\eta} = -2F(\eta), \tag{18}$$

$$\frac{d^2F(\eta)}{d\eta^2} = \frac{1}{\epsilon_5}\left(\frac{\epsilon_4}{\epsilon_2} MF(\eta) - \lambda_1(1+\lambda_2\theta(\eta))\theta(\eta) + F(\eta)^2 + H(\eta)\frac{dF(\eta)}{d\eta} - G(\eta)^2\right), \tag{19}$$

$$\frac{d^2G(\eta)}{d\eta^2} = \frac{1}{\epsilon_5}\left(2F(\eta)G(\eta) + \frac{dG(\eta)}{d\eta}H(\eta) + \frac{\epsilon_4}{\epsilon_2}M(\eta)G(\eta)\right), \tag{20}$$

$$\begin{aligned}\frac{d^2\theta(\eta)}{d\eta^2} = {} & \frac{\widetilde{R}}{\epsilon_1 Pr}\left[(\theta_\omega - 1)^3\left(3\theta(\eta)^2\left(\frac{d\theta(\eta)}{d\eta}\right)^2 + \frac{d^2\theta(\eta)}{d\eta^2}(\theta(\eta))^3\right)\right] \\ & + Pr\frac{\epsilon_1}{\epsilon_3}\frac{d\theta(\eta)}{d\eta}H(\eta) + \frac{\widetilde{R}}{\epsilon_1 Pr}\left[3(\theta_\omega - 1)^2\left(2\left(\frac{d\theta(\eta)}{d\eta}\right)^2\theta(\eta) + \frac{d^2\theta(\eta)}{d\eta^2}\theta(\eta)^2\right)\right] \\ & + \frac{\widetilde{R}}{\epsilon_1 Pr}\left[3(\theta_\omega - 1)\left(\left(\frac{d\theta(\eta)}{d\eta}\right)^2 + \frac{d\theta(\eta)}{d\eta}\theta(\eta)\right) + \frac{d^2\theta(\eta)}{d\eta^2}\right] - \frac{\epsilon_4}{\epsilon_1}MEc\left(F(\eta)^2 + G(\eta)^2\right),\end{aligned} \tag{21}$$

For numerical solution we make following substitutions as [39]

$$\begin{aligned}& q_1 = F(\eta),\ q_2 = q_1' = \frac{dF(\eta)}{d\eta},\ q_3 = G(\eta),\ q_4 = q_3' = \frac{dG(\eta)}{d\eta}, \\ & q_5 = H(\eta),\ q_6 = \theta(\eta),\ q_7 = q_6' = \frac{d\theta(\eta)}{d\eta}\end{aligned} \tag{22}$$

this transforms (18)–(21) and boundary conditions (12) as follows

$$\begin{aligned}& q_1' = q_2, q_2' = \frac{1}{\epsilon_5}\left(\frac{\epsilon_4}{\epsilon_2}Mq_1 - \lambda_1(1+\lambda_2 q_6)q_6 + q_1^2 + q_5 q_2 - q_3^2\right)q_3' = q_4, q_4' \\ & = \frac{1}{\epsilon_5}\left(2q_1q_3 + q_4q_5 + \frac{\epsilon_4}{\epsilon_2}M(\eta)q_3\right), q_5' = -2q_1, q_6' = q_7, q_7' \\ & = Pr\frac{\epsilon_1}{\epsilon_3}q_7q_5 + \frac{\widetilde{R}}{\epsilon_1 Pr} \\ & \quad \times\left[(\theta_\omega - 1)^3(3q_6^2q_7^2 + q_7'q_6^3) + 3(\theta_\omega - 1)^2(2q_7^2q_6 + q_7'q_6^2) + 3(\theta_\omega - 1)(q_7^2 + q_6q_7) + q_7'\right] \\ & \quad - \frac{\epsilon_4}{\epsilon_1}MEc(q_1^2 + q_3^2),\end{aligned} \tag{23}$$

with boundary conditions

$$\begin{aligned}& q_1(0) = \gamma_1 q_2(0), \quad q_3(0) = 1, \quad q_5(0) = W_s \quad q_6(0) = 1 + \gamma_2 q_7(0), \\ & q_1(1) = 0, \quad q_3(1) = 0, \quad q_6(1) = 0,\end{aligned} \tag{24}$$

The complete algorithm for solution technique through Fehlberg Runge–Kutta method is depicted in Fig. 2. Approximate solutions ($\widetilde{H}, \widetilde{F}, \widetilde{G}$ and $\widetilde{T}$) are obtained as a result.

4.2. Validation process

The obtained results are validated in three different ways as follows:

Numerical Validation through Solution Uncertainty

Approximate solutions are further validated by computation of numerical uncertainties in the results. Numerical uncertainty $\mathfrak{U}_c$ is given as

$$\mathfrak{U}_c = \sqrt{\frac{\sum(Sol_i - \mu_i)^2}{n(n-1)}} \tag{25}$$

where $i = 1(1)4$ for four set of solutions, n is the number of iterations and μ_i is the mean of n iterations. Solutions along with numerical uncertainties are presented in Table 2 for fixed values of fluid parameters. The results reveal that the uncertainty in approximate solutions lie between $\pm 0.1\% - \pm 9.5\%$.

Numerical Validation by Absolute Residual Errors

In order to validate the results, approximate solutions are used in Eqs. (18)–(21) to obtain the residual errors as

$$\begin{aligned}& \mathbb{R}_1 = \widetilde{H}_\eta + 2\widetilde{F}, \mathbb{R}_2 = \widetilde{F}_{\eta,\eta} - \frac{1}{\epsilon_5}\left(M\widetilde{F} - \lambda_1\left(1 + \lambda_2\widetilde{T}\right)\widetilde{T} + \widetilde{F}^2 + \widetilde{H}\widetilde{F}_\eta - \widetilde{G}^2\right), \mathbb{R}_3 \\ & = 2\widetilde{F}\widetilde{G} + \widetilde{H}\widetilde{G}_\eta - \epsilon_5\widetilde{G}_{\eta,\eta} + \frac{\epsilon_4}{\epsilon_2}M\widetilde{G}, \mathbb{R}_4 \\ & = \frac{1}{Pr}\frac{\epsilon_3}{\epsilon_1}\widetilde{T}_{\eta,\eta} - H\widetilde{T}_\eta - \frac{\widetilde{R}}{\epsilon_1 Pr} \\ & \quad \times\left[(\theta_\omega - 1)^3\left(3\widetilde{T}^2\widetilde{T}_\eta^2 + \widetilde{T}_{\eta,\eta}\widetilde{T}^3\right) + 3(\theta_\omega - 1)^2\left(2\widetilde{T}\widetilde{T}_\eta^2 + \widetilde{T}^2\widetilde{T}_{\eta,\eta}\right) + 3(\theta_\omega - 1)\left(\widetilde{T}_\eta^2 + \widetilde{T}\widetilde{T}_\eta\right) + \widetilde{T}_{\eta,\eta}\right] \\ & \quad + \frac{\epsilon_4}{\epsilon_1}MEc\left(F^2 + G^2\right),\end{aligned} \tag{26}$$

The absolute residual errors $\mathbb{R}_1, \mathbb{R}_2, \mathbb{R}_3, \mathbb{R}_4$ and average absolute residual errors $\mathbb{R}_{avg}$ are presented in Table 3. The averaged residual errors range from 10^{-4} to 10^{-7} which depicts promising results in terms of accuracy.

Validation with Experimental Results

Furthermore, the obtained solutions are validated in Fig. 3 with experimental data presented by Kim et al. [40]. It is

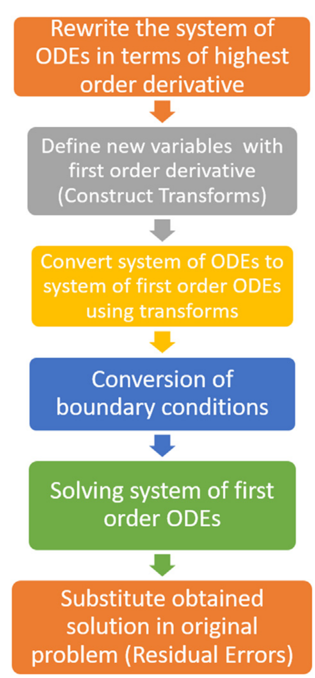

Fig. 2 Solution algorithm and validation process.

Table 2 Solutions through Fehlberg Runge–Kutta Method when $Pr = 2.7, Ec = 0.8, M = 2.7, \lambda_1 = \lambda_2 = 10, \widetilde{R} = 1.1, \theta_\omega = 1.8, \varphi = 0.05$ and $W_s = 2.5$.

η	$\widetilde{H}$	$\widetilde{F}$	$\widetilde{G}$	$\widetilde{T}$
0.0	2.5	0.222492	1.	−0.0124171
0.1	2.45542	0.222553	0.918506	−0.00979238
0.2	2.41125	0.218511	0.840114	−0.00749689
0.3	2.36828	0.210542	0.763561	−0.00553655
0.4	2.3273	0.198605	0.687082	−0.00389051
0.5	2.28912	0.182402	0.608227	−0.00254538
0.6	2.25466	0.161341	0.523591	−0.00149423
0.7	2.22497	0.134452	0.428436	−0.00073376
0.8	2.20137	0.100264	0.316171	−0.000257242
0.9	2.1855	0.0565683	0.177616	−0.0000387897
1.0	2.17959	0.	0.	0.
$\mathfrak{U}_c$	±0.0339	±0.0226	±0.0952	±0.00129

observed that the results obtained from present study are in a good agreement with experimental results in literature.

5. Results and discussion

In this section graphical analysis is presented briefly for various fluid parameters in case of radial, tangential, axial velocity and temperature separately. Skin friction and Nusselt number are also analyzed at both walls.

5.1. Radial velocity

In Fig. 4 behavior of radial velocity component, $F(\eta)$, is presented against various parameters for volume fraction, $\varphi = 0.1$. Fig. 4(a) depicts decreasing radial velocity as magnetic interaction parameter increases. As M increases, drag force enhances in fluid flow causing depleted velocity in radial direction. Parameter of suction injuction, W_s, elevates fluid flow Fig. 4(b) as positive values indicate injuction, causing greater fluid inflow. With increase in velocity slip parameter, γ_1, radial velocity increases Fig. 4(d). Increase in both linear and non-linear mixed convection parameters, λ_1 and λ_2, respectively, raises the fluid flow in radial direction as seen in Fig. 4(d) and 4(e). As volume fraction of radioactive material in base fluid increases Fig. 4(f), velocity also increases causing greater flow than usual in blood arteries in radial direction.

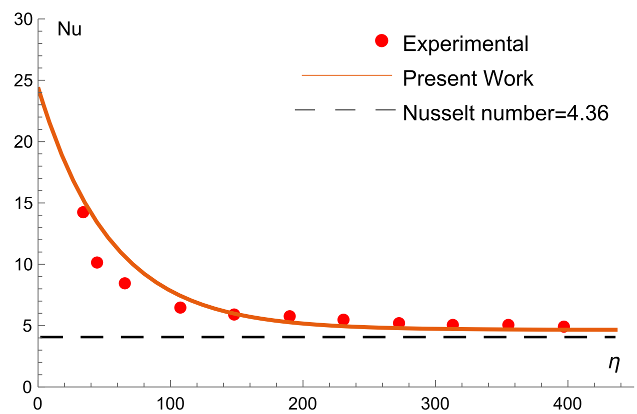

Fig. 3 Comparison of present results with experimental data [40].

Table 3 Residual Errors $\mathbb{R}_i$, where $i = 1(1)4$, using Fehlberg Runge–Kutta Method.

η	$\mathbb{R}_1$	$\mathbb{R}_2$	$\mathbb{R}_3$	$\mathbb{R}_4$	$\mathbb{R}_{avg}$
0.0	2.70×10^{-6}	7.98×10^{-4}	3.81×10^{-5}	4.43×10^{-4}	3.20×10^{-4}
0.1	2.84×10^{-7}	5.42×10^{-5}	2.42×10^{-6}	1.46×10^{-5}	1.79×10^{-5}
0.2	6.64×10^{-8}	8.69×10^{-6}	3.64×10^{-7}	1.58×10^{-6}	2.67×10^{-6}
0.3	2.63×10^{-8}	2.24×10^{-6}	8.95×10^{-8}	3.83×10^{-7}	6.86×10^{-7}
0.4	1.59×10^{-8}	7.37×10^{-7}	2.99×10^{-8}	1.59×10^{-7}	2.36×10^{-7}
0.5	1.40×10^{-8}	1.39×10^{-7}	1.10×10^{-8}	1.03×10^{-7}	6.68×10^{-8}
0.6	1.79×10^{-8}	4.78×10^{-7}	1.59×10^{-9}	1.00×10^{-7}	1.49×10^{-7}
0.7	3.34×10^{-8}	2.21×10^{-6}	4.88×10^{-9}	1.46×10^{-7}	5.98×10^{-7}
0.8	9.58×10^{-8}	1.07×10^{-5}	2.26×10^{-8}	3.32×10^{-7}	2.79×10^{-6}
0.9	4.64×10^{-7}	8.02×10^{-5}	7.44×10^{-7}	1.29×10^{-6}	2.06×10^{-5}
1.0	5.03×10^{-6}	1.42×10^{-4}	2.59×10^{-5}	1.15×10^{-5}	3.65×10^{-4}

5.2. Tangential velocity

Fig. 5 presents effects of M, W_s, γ_1, λ_1, λ_2 and φ on tangential velocity, $G(\eta)$. Increase in M decreases velocity in tangential direction (see Fig. 5(a)) while W_s increases the velocity in Fig. 5(b) similar to radial component. As velocity slip γ_1 increases in Fig. 5(c), the fluid flow slows down tangentially in contrast to radial direction due to slip parameter being introduced in radial direction only. With higher linear and non-linear mixed convection parameters in Fig. 5(d) and 5 (e), flow of nanofluid in tangential direction slows down. Increasing volume fraction φ as observed in Fig. 5(f) increases nanofluid velocity along the tangent.

5.3. Axial velocity

Graphical analysis on axial velocity $H(\eta)$ is done in Fig. 6. M and W_s both increase the flow of fluid in axial direction as depicted in Figs. 6a) and Graphs:H(b). Velocity slip decreases nanofluid flow in axial direction (see Fig. 6(c)) just as in tangential direction due to slip parameter introduced radially. λ_1 and λ_2 decreases axial velocity also. With increasing volume

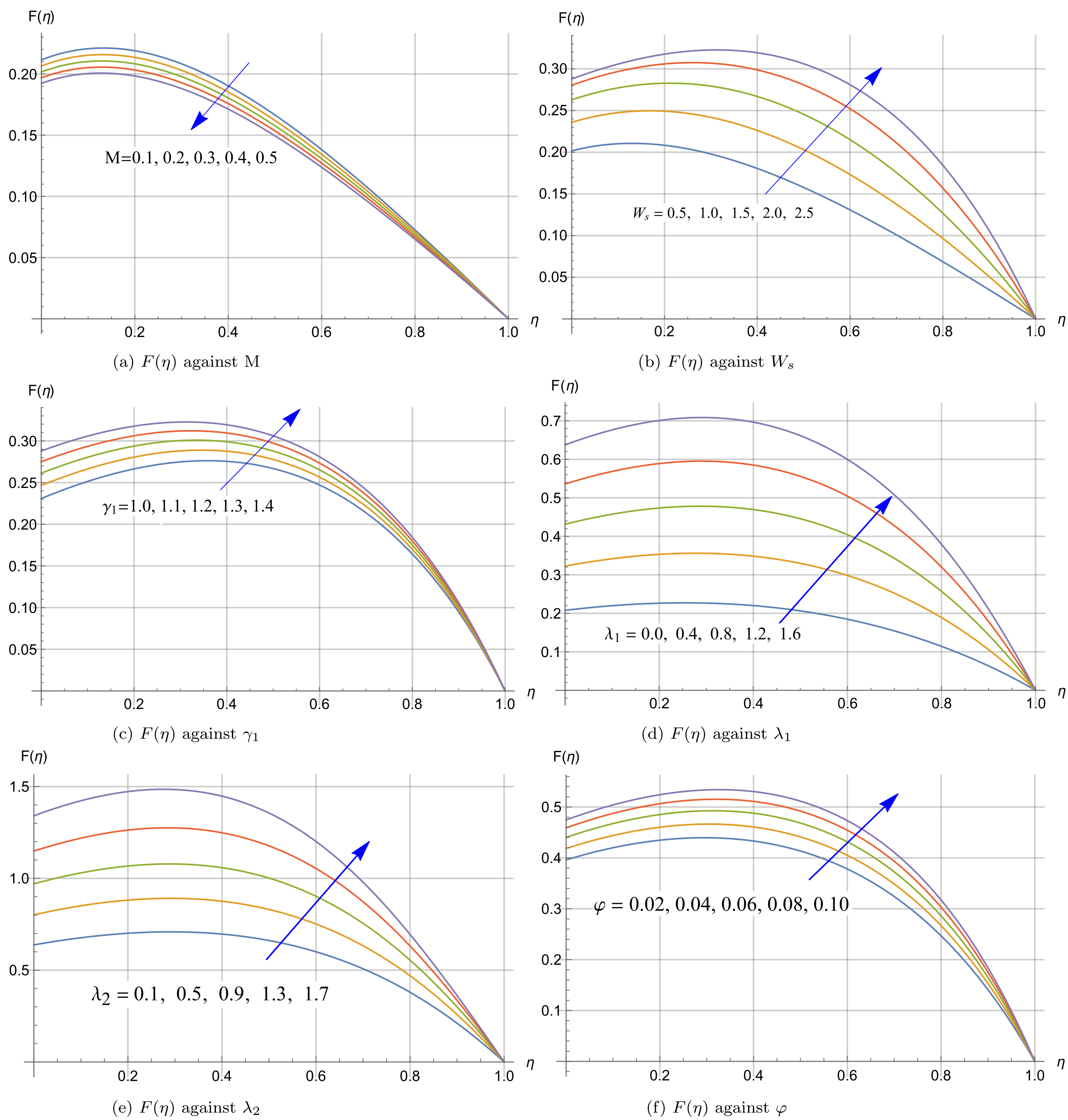

(a) $F(\eta)$ against M

(b) $F(\eta)$ against W_s

(c) $F(\eta)$ against γ_1

(d) $F(\eta)$ against λ_1

(e) $F(\eta)$ against λ_2

(f) $F(\eta)$ against φ

Fig. 4 Effect of various parameters on the radial velocity.

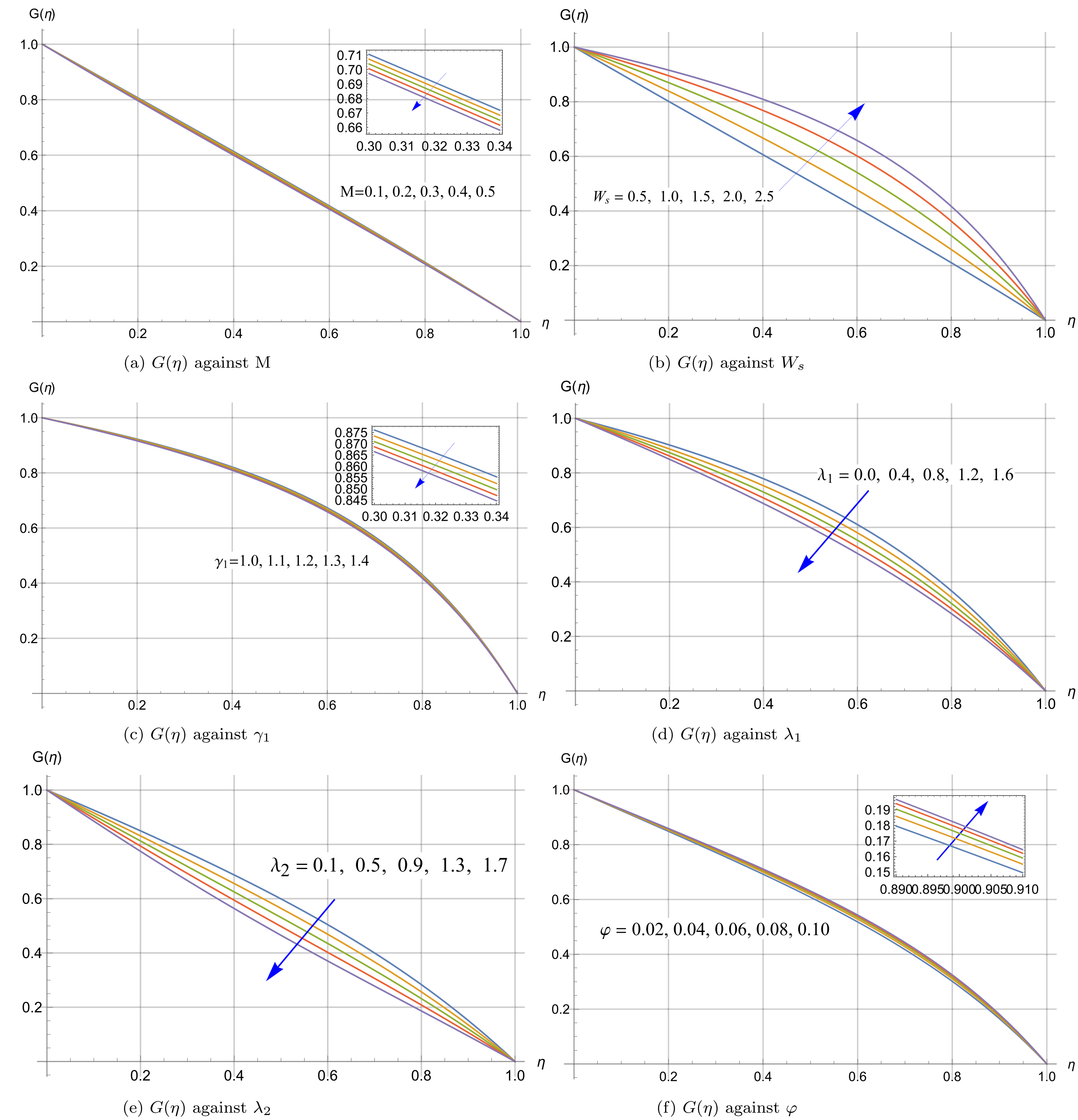

(a) $G(\eta)$ against M
(b) $G(\eta)$ against W_s
(c) $G(\eta)$ against γ_1
(d) $G(\eta)$ against λ_1
(e) $G(\eta)$ against λ_2
(f) $G(\eta)$ against φ

Fig. 5 Effect of various parameters on tangential velocity for $\varphi = 0.1$.

fraction in nanofluid, the axial velocity is observed to decrease in contrast to radial and tangential direction in Fig. 6(f).

5.4. Temperature Profile

Behavior of nanofluid temperature for various fluid parameters can be observed in.

Fig. 7. In Fig. 7(a), magnetic interaction M increases the fluid temperature. As increasing M produces Lorentz like drag force which offers resistance to fluid flow resulting in elevated temperature profile. Increase in fluid injection in Fig. 7(b) decreases blood temperature as more fluid flows and heat transfer takes place. Velocity slip γ_1 increases temperature in Fig. 7(c) while temperature slip γ_2 decreases temperature in Fig. 7(d). Linear and non-linear mixed convection parameters λ_1 and λ_2, respectively, show both increasing and decreasing temperature profile about a point as depicted in Figs. 7(e) and 7(f). In case of λ_1, blood temperature rises before

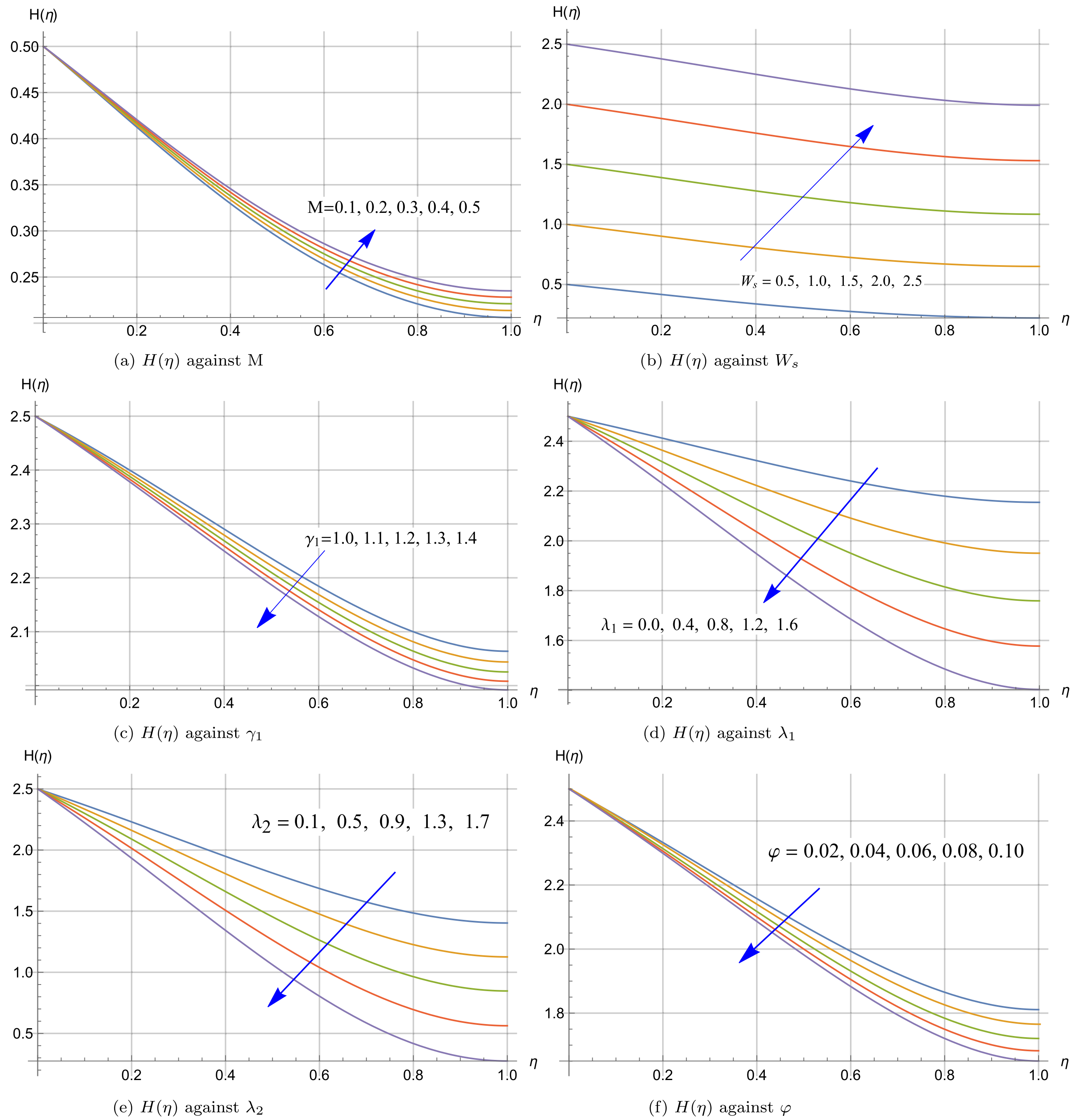

(a) $H(\eta)$ against M (b) $H(\eta)$ against W_s

(c) $H(\eta)$ against γ_1 (d) $H(\eta)$ against λ_1

(e) $H(\eta)$ against λ_2 (f) $H(\eta)$ against φ

Fig. 6 Effect of various parameters on axial velocity for $\varphi = 0.1$.

$\eta = 0.84$, whereas it declines afterwards. For λ_2, temperature increases before $\eta = 0.75$ and decreases onwards. Non-linear radiation parameter $\widetilde{R}$, increases temperature of blood nanofluid in Fig. 7(g). Fig. 7(h) shows blood temperature for increasing volume fraction φ of nanoparticles in blood. With increasing φ, blood nanofluid temperature falls before $\eta = 0.85$, and it increases for $\eta > 0.85$.

5.5. Skin Friction and Nusselt Number

In Figs. 8 and 9, skin friction and Nusselt number are plotted against a range of nanoparticle volume fraction φ on both walls for comprehensive analysis with and without slip conditions. Moreover, skin friction and heat transfer rates for three nanoparticles UO_2, ThO_2 and Rd are compared graphically. Skin friction shows increasing while heat transfer rate shows decreasing behavior as φ on y-axis increases. With increasing volume fraction more resistance to flow causes higher skin friction and hence lower heat transfer rate. In Fig. 8(a), Rd offers highest skin friction with slip at wall $\eta = 0$, whereas without slip in Fig. 8(b), Rd offers least skin friction. Fig. 9(a) depicts highest heat transfer rate for ThO_2 as it has the highest thermal conductivity k in Table 1. Without slip in Fig. 9(b) behavior of heat transfer

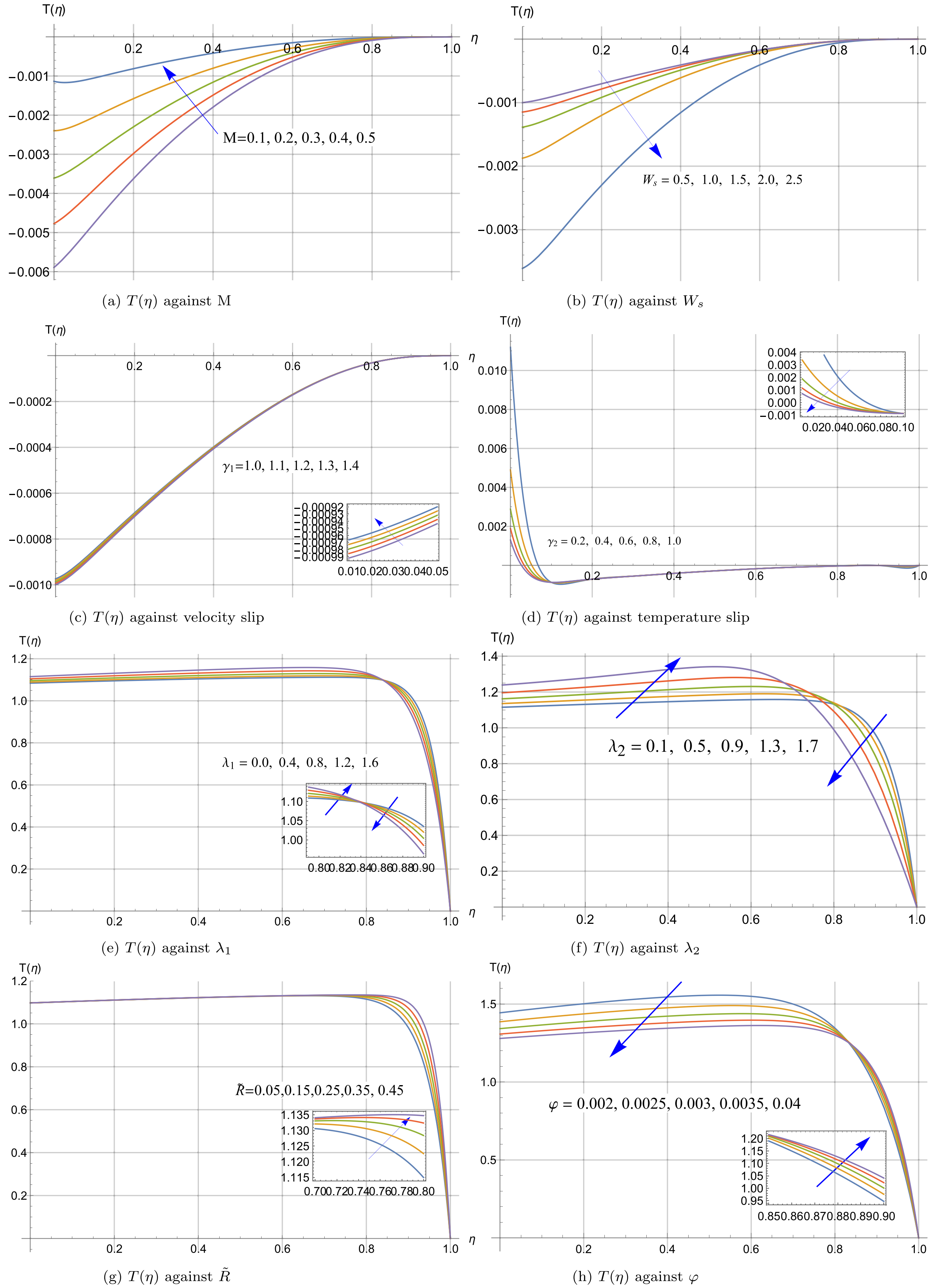

Fig. 7 Effect of various parameters on temperature profile for $\varphi = 0.1$.

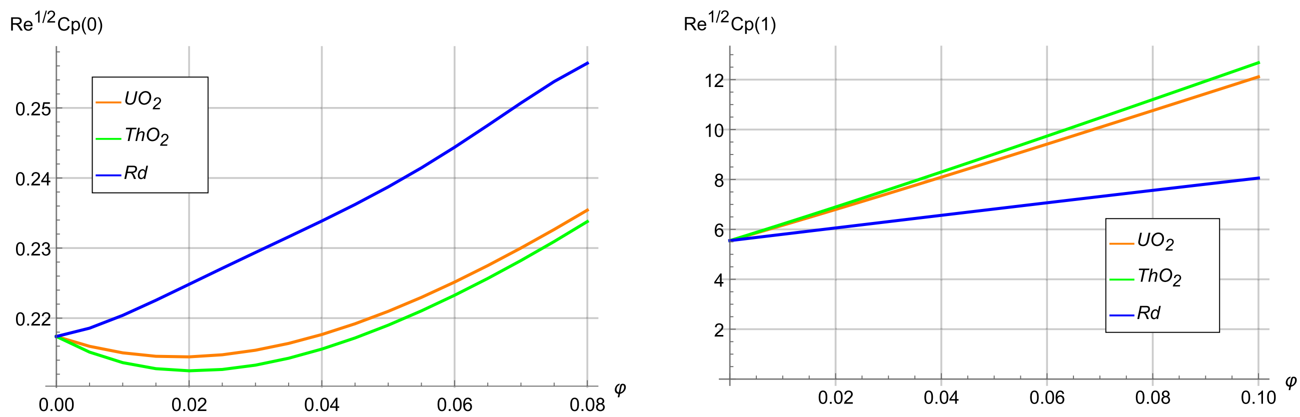

(a) Skin friction at $\eta = 0$ (b) Skin friction at $\eta = 1$

Fig. 8 Skin friction at both walls.

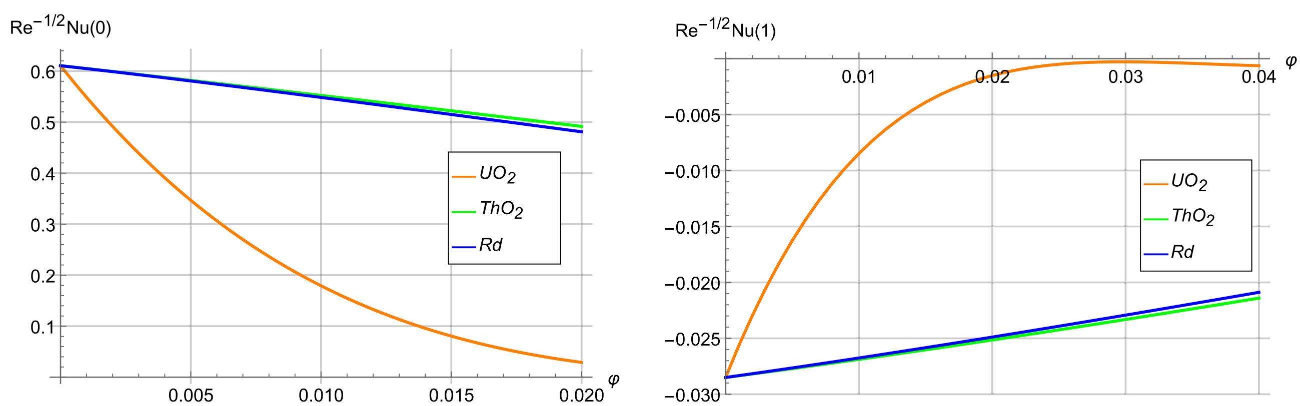

(a) Heat transfer at $\eta = 0$ (b) Heat transfer at $\eta = 1$

Fig. 9 Heat transfer rate at both walls.

rate is totally opposite. Hence skin friction and Nusselt number have entirely contrasting results on both walls.

5.6. Contour analysis

The physical analysis of current study is further simulated through contour plots in Figs. 10–12. In Fig. 10(a) radial velocity increases rapidly for slip parameter γ_1 values between 0 and 1 whereas increase is not much prominent for higher values of γ_1. Tangential velocity in Fig. 10(b) is higher for smaller values of η and it decreases with increasing η. Fig. 10(c) reveals that injuction increases the axial velocity while suction decreases the blood flow in axial direction. Suction results in movement of fluid particles towards the wall and consequently decreases the velocity boundary layer. Temperature of blood becomes higher when thermal slip increases. Contour spacing shows that the increase in temperature is more prominent in case of lower values of thermal slip when compared with higher values. In Fig. 11 skin friction is simulated against increasing Reynolds number Re and volume fraction φ of three types of nanoparticles, $UO_2, /, ThO_2$ and Rd in blood. For lower Reynolds number increase in skin friction is more rapid than higher values in all cases of nanoparticles. Higher Re results in more turbulent flow which increases skin friction as a result. Rd offers least skin friction in comparison with UO_2 and ThO_2. Fig. 12 depicts that rate of heat transfer is enhanced when flow behavior changes from laminar to turbulent (i.e. $Re > 2300$). Moreover, it is also observed that Rd and ThO_2 offers more heat transfer than UO_2 nanoparticles in blood. This is due to the fact that Rd and ThO_2 nanoparticles have higher thermal conductivity than UO_2.

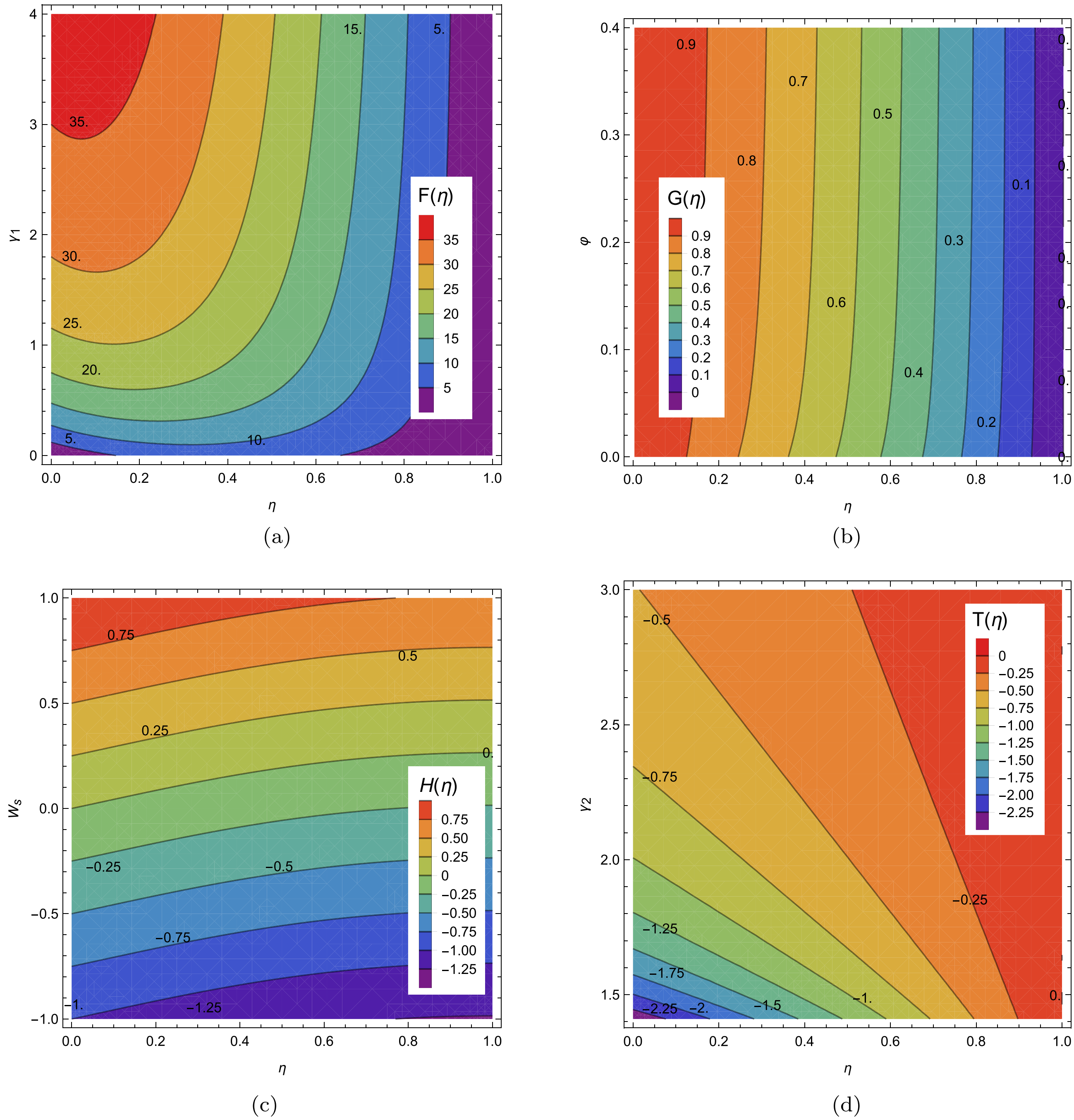

Fig. 10 Impact of (a) Velocity slip on radial velocity, (b) Volume fraction on tangential velocity, (c) Suction/Injuction parameter on axial velocity, (d) Thermal slip on temperature.

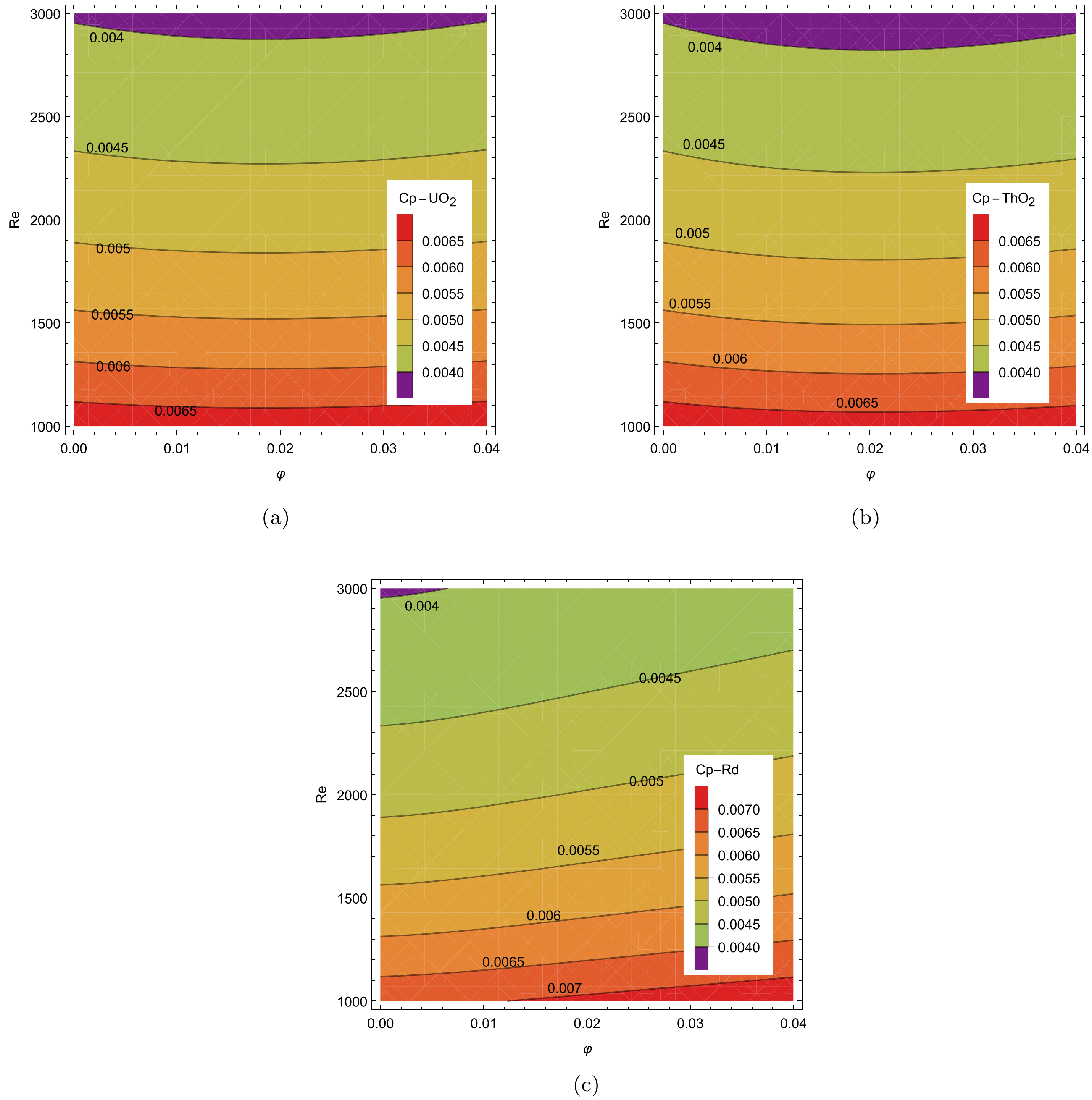

Fig. 11 Impact of Reynolds number and volume fraction on skin friction at wall in case of (a) UO_2 nanoparticles, (b) ThO_2 nanoparticles, (c) *Rd* nanoparticles.

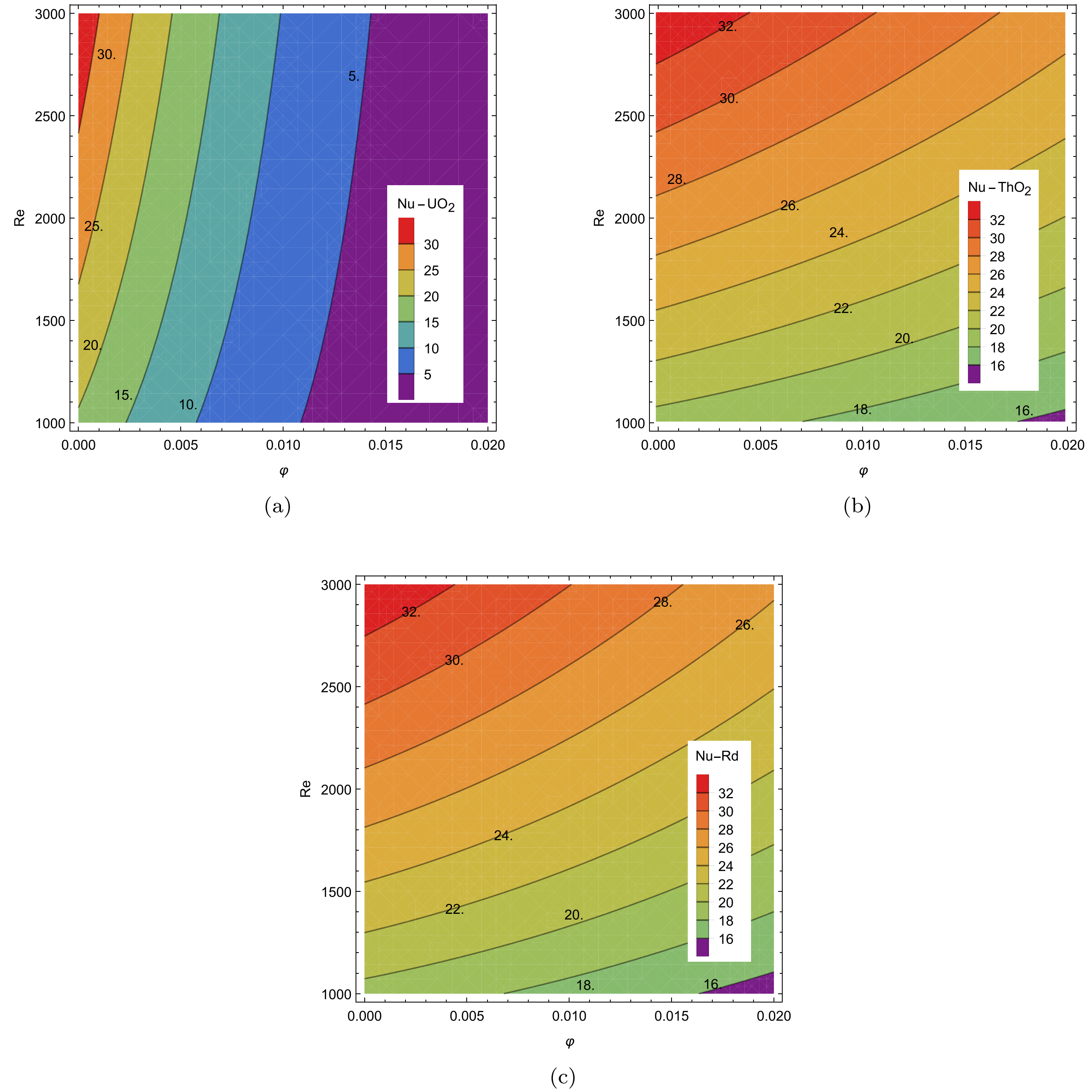

Fig. 12 Impact of Reynolds number and volume fraction on heat transfer rate in case of (a) UO_2 nanoparticles, (b) ThO_2 nanoparticles, (c) *Rd* nanoparticles.

6. Conclusion

Many scientists in nuclear facilities, and workers in medical and industrial sectors are facing health related issues while exposing to nuclear radiations. Due to this reason, it is of great importance to model and analyze such effects on blood profiles. Blood nanofluid have been investigated in earlier studies mentioned in Section 1, but none of those analyze the effect of radioactive elements on the blood. To fill this gap, this article presents the modeling and simulation of blood-nanofluid to depict three types of radioactive nanoparticles, UO_2, ThO_2 and *Rd*. Validity and convergence of the obtained solution is checked through absolute residual errors after numerically simulating the modeled problem using Fehlberg Runge–Kutta algorithm. Obtained results are further validated by comparison with experimental data. Furthermore, numerical uncertainties are also computed for approximate solutions. Graphical analysis through 2D plots and contours reveals following key findings of this study:

- Increase in volume fraction φ increases nanofluid velocity in radial and tangential direction.

- Temperature profile decreases when $0 < \eta < 0.85$, while opposite (increasing) behavior is observed when $0.85 < \eta < 1$.
- *Rd* nanoparticles offer maximum skin friction and heat transfer rate at wall $\eta = 0$ and hence can be used for the treatment of cancer and maligns.
- Rapid increase in radial velocity $F(\eta)$ is observed for slip parameter between 0 and 1.
- Nanofluid temperature shows a drastic increase when thermal slip rises from 0.0 to 2.0.
- Higher values of Reynolds number *Re* results in elevated skin friction and heat transfer rate.
- UO_2 shows highest skin friction and lowest heat transfer rate when compared with ThO_2 and *Rd* against increasing turbulence in the nanofluid flow.

Declaration of Competing Interest

The authors declare that they have no known competing financial interests or personal relationships that could have appeared to influence the work reported in this paper.

References

[1] M.M. Bhatti, A. Shahid, T. Abbas, S.Z. Alamri, R. Ellahi, Study of activation energy on the movement of gyrotactic microorganism in a magnetized nanofluids past a porous plate, Processes 8 (3) (2020) 328, Mar.
[2] S.M. Hussain, W. Jamshed, A comparative entropy based analysis of tangent hyperbolic hybrid nanofluid flow: Implementing finite difference method, Int. Commun. Heat Mass Transfer 129 (2021) 105671, Dec.
[3] R.J. Punith Gowda, R. Naveen Kumar, B.C. Prasannakumara, B. Nagaraja, B.J. Gireesha, Exploring magnetic dipole contribution on ferromagnetic nanofluid flow over a stretching sheet: An application of stefan blowing, J. Mol. Liq., 335:116215, Aug 2021.
[4] H.T. Basha and R. Sivaraj. Numerical simulation of blood nanofluid flow over three different geometries by means of gyrotactic microorganisms: Applications to the flow in a circulatory system, Proc. Inst. Mech. Eng., Part C: J. Mech. Eng. Sci., 235(2) (2020) 441–460.
[5] W. Alghamdi, A. Alsubie, P. Kumam, A. Saeed, T. Gul, MHD hybrid nanofluid flow comprising the medication through a blood artery, Scient. Rep., 11(1), June 2021.
[6] Z. Shah, A. Khan, W. Khan, M.K. Alam, S. Islam, P. Kumam, P. Thounthong, Micropolar gold blood nanofluid flow and radiative heat transfer between permeable channels, Comput. Methods Programs Biomed. 186 (2020) 105197. Apr.
[7] N. Biswas, D.K. Mandal, N.K. Manna, A.C. Benim, Magneto-hydrothermal triple-convection in a w-shaped porous cavity containing oxytactic bacteria, Scient. Rep. 12 (1) (2022), Oct.
[8] H.S. Chahregh, S. Dinarvand, Tio-ag/blood hybrid nanofluid flow through an artery with applications of drug delivery and blood circulation in the respiratory system, Int. J. Numer. Methods Heat Fluid Flow 30 (11) (2020) 4775–4796, Jan.
[9] O. Prakash, S.P. Singh, D. Kumar, Y.K. Dwivedi, A study of effects of heat source on MHD blood flow through bifurcated arteries, AIP Advances 1 (4) (2011) 042128, Dec.
[10] P. Barnoon, M. Ashkiyan, Magnetic field generation due to the microwaves by an antenna connected to a power supply to destroy damaged tissue in the liver considering heat control, J. Magn. Magn. Mater. 513 (2020) 167245, Nov.
[11] M.K. Mondal, N. Biswas, A. Datta, B.K. Sarkar, N.K. Manna, Positional impacts of partial wall translations on hybrid nanofluid flow in porous media: Real coded genetic algorithm (RCGA), Int. J. Mech. Sci. 217 (2022) 107030, Mar.
[12] S.A. Khan, T. Hayat, M.I. Khan, A. Alsaedi, Salient features of dufour and soret effect in radiative MHD flow of viscous fluid by a rotating cone with entropy generation, Int. J. Hydrogen Energy 45 (28) (2020) 14552–14564, May.
[13] D.K. Mandal, N. Biswas, N.K. Manna, D.K. Gayen, R.S.R. Gorla, A.J. Chamkha, Thermo-fluidic transport process in a novel m-shaped cavity packed with non-darcian porous medium and hybrid nanofluid: Application of artificial neural network (ANN), Phys. Fluids 34 (3) (2022) 033608, Mar.
[14] P. Barnoon, D. Toghraie, F. Eslami, B. Mehmandoust, Entropy generation analysis of different nanofluid flows in the space between two concentric horizontal pipes in the presence of magnetic field: Single-phase and two-phase approaches, Comput. Math. Appl. 77 (3) (2019) 662–692, Feb.
[15] N.S. Anuar, N. Bachok, M. Turkyilmazoglu, N.M. Arifin, H. Rosali, Analytical and stability analysis of MHD flow past a nonlinearly deforming vertical surface in carbon nanotubes, Alexandria Eng. J. 59 (1) (2020) 497–507, Feb.
[16] W.F. Xia, S. Ahmad, M.N. Khan, H. Ahmad, A. Rehman, J. Baili, T.N. Gia, Heat and mass transfer analysis of nonlinear mixed convective hybrid nanofluid flow with multiple slip boundary conditions, Case Stud. Therm. Eng. 32 (2022) 101893. Apr.
[17] W. Ibrahim, C. Zemedu, MHD nonlinear mixed convection flow of micropolar nanofluid over nonisothermal sphere, Math. Probl. Eng., 1–20, June 2020.
[18] D.K. Mandal, N. Biswas, N.K. Manna, R.S.R. Gorla, A.J. Chamkha, Hybrid nanofluid magnetohydrodynamic mixed convection in a novel w-shaped porous system, Int. J. Numer. Methods for Heat and Fluid Flow, Aug 2022.
[19] M. Irfan, W.A. Khan, M. Khan, M. Mudassar Gulzar, Influence of arrhenius activation energy in chemically reactive radiative flow of 3d carreau nanofluid with nonlinear mixed convection, J. Phys. Chem. Solids, 125 (2019) 141–152 .
[20] N.K. Manna, D.K. Mandal, N. Biswas, R.S.R. Gorla, Magneto-thermal convection of hybrid nanofluid in a non-darcian porous complex wavy enclosure, Eur. Phys. J. Special Top. (2022).
[21] T. Hayat, F. Haider, A. Alsaedi, Darcy-forchheimer flow with nonlinear mixed convection, Appl. Math. Mech. 41 (11) (2020) 1685–1696, Oct.
[22] M. Ramzan, J.D. Chung, N. Ullah, Radiative magnetohydrodynamic nanofluid flow due to gyrotactic microorganisms with chemical reaction and non-linear thermal radiation, Int. J. Mech. Sci., 130 (2017) 31–40.
[23] K.G. Kumar, N.G. Rudraswamy, B.J. Gireesha, S. Manjunatha, Non linear thermal radiation effect on williamson fluid with particle-liquid suspension past a stretching surface, Results Phys. 7 (2017) 3196–3202.
[24] S. Muhammad, G. Ali, Z. Shah, S. Islam, S. Hussain, The rotating flow of magneto hydrodynamic carbon nanotubes over a stretching sheet with the impact of non-linear thermal radiation and heat generation/absorption, Appl. Sci. 8 (4) (2018) 482, Mar.
[25] S.S. Ghadikolaei, K. Hosseinzadeh, D.D. Ganji, Numerical study on magnetohydrodynic CNTs-water nanofluids as a micropolar dusty fluid influenced by non-linear thermal radiation and joule heating effect, Powder Technol. 340 (2018) 389–399, Dec.
[26] Y.X. Li, H. Waqas, K.A. Khaled, S.A. Khan, M.I. Khan, S.U. Khan, R. Naseem, Y.M. Chu, Simultaneous features of wu's slip, nonlinear thermal radiation and activation energy in unsteady bio-convective flow of maxwell nanofluid configured by a stretching cylinder, Chin. J. Phys. 73 (2021) 462–478, Oct.

[27] T. Muhammad, H. Waqas, U. Farooq, M.S. Alqarni, Numerical simulation for melting heat transport in nanofluids due to quadratic stretching plate with nonlinear thermal radiation, Case Stud. Therm. Eng. 27 (2021) 101300, Oct.

[28] P. Barnoon, Numerical assessment of heat transfer and mixing quality of a hybrid nanofluid in a microchannel equipped with a dual mixer, Int. J. Thermofluids 12 (2021) 100111, Nov.

[29] M. Imran, U. Farooq, T. Muhammad, S.U. Khan, H. Waqas, Bioconvection transport of carreau nanofluid with magnetic dipole and nonlinear thermal radiation, Case Studies in Thermal Engineering 26 (2021) 101129. Aug.

[30] Y.Q. Song, S.A. Khan, M. Imran, H. Waqas, S.U. Khan, M.I. Khan, S. Qayyum, Y.M. Chu, Applications of modified darcy law and nonlinear thermal radiation in bioconvection flow of micropolar nanofluid over an off centered rotating disk, Alexandria Engineering Journal 60 (5) (2021) 4607–4618, Oct.

[31] M.I. Khan, H. Waqas, S.U. Khan, M. Imran, Y.M. Chu, A. Abbasi, S. Kadry, Slip flow of micropolar nanofluid over a porous rotating disk with motile microorganisms, nonlinear thermal radiation and activation energy, Int. Commun. Heat Mass Transfer 122 (2021) 105161, Mar.

[32] P. Barnoon, F. Bakhshandehfard, Thermal management in a biological tissue in order to destroy tissue under local heating process, Case Studies in Thermal Engineering 26 (2021) 101105. Aug.

[33] M. Bilal, M. Ramzan, Y. Mehmood, M.K. Alaoui, and R. Chinram. An entropy optimization study of non-darcian magnetohydrodynamic williamson nanofluid with nonlinear thermal radiation over a stratified sheet. Proceedings of the Institution of Mechanical Engineers, Part E: Journal of Process Mechanical Engineering, 235(6), 1883–1894, jun 2021.

[34] T. Sajid, W. Jamshed, F. Shahzad, M.A. Aiyashi, M.R. Eid, K. S. Nisar, A. Shukla, Impact of maxwell velocity slip and smoluchowski temperature slip on CNTs with modified fourier theory: Reiner-philippoff model, PLOS ONE 16 (10) (2021) e0258367, Oct.

[35] M. Khan, A. Rasheed, Slip velocity and temperature jump effects on molybdenum disulfide mos2 and silicon oxide sio2 hybrid nanofluid near irregular 3d surface, Alexandria Engineering Journal 60 (1) (2021) 1689–1701, Feb.

[36] P.Y. Xiong, M. Nazeer, F. Hussain, M.I. Khan, A. Saleem, S. Qayyum, Y.M. Chu, Two-phase flow of couple stress fluid thermally effected slip boundary conditions: Numerical analysis with variable liquids properties, Alexandria Eng. J. 61 (5) (2022) 3821–3830, May.

[37] T. Hayat, S.A. Khan, A. Alsaedi, Irreversibility characterization in nanoliquid flow with velocity slip and dissipation by a stretchable cylinder, Alexandria Eng. J., 60(3), 2835–2844, jun 2021.

[38] S. Srinivas, A. Vijayalakshmi, A.S. Reddy, Flow and heat transfer of gold-blood nanofluid in a porous channel with moving/stationary walls, J. Mech. 33 (3) (2016) 395–404, Nov.

[39] U. Ali, M.Y. Malik, A.A. Alderremy, S. Aly, and K.U. Rehman. A generalized findings on thermal radiation and heat generation/absorption in nanofluid flow regime, Phys. A: Stat. Mech. Its Appl., 553 (2020) 124026.

[40] D. Kim, Y. Kwon, Y. Cho, C. Li, S. Cheong, Y. Hwang, J. Lee, D. Hong, S. Moon, Convective heat transfer characteristics of nanofluids under laminar and turbulent flow conditions, Curr. Appl. Phys. 9 (2) (2009) e119–e123, Mar.